Journal of Raman Spectroscopy

WILEY

Journal of RAMAN SPECTROSCOPY

RESEARCH ARTICLE

Thermal Degradation Threshold in Ag@Chondroitin Sulfate Memristors Revealed by Temperature-Resolved Raman Spectroscopy

Alfredo Antonio Alencar Exposito De Queiroz[1,2] | Marcelo Barbosa de Andrade[1,3] |
Alvaro Antonio Alencar de Queiroz[4]

[1]São Carlos Institute of Physics, University of São Paulo, São Carlos, Brazil | [2]Instituto Tecnológico de Aeronáutica, Campus do CTA, São José dos Campos, São Paulo, Brazil | [3]Department of Physics, Federal University of Ouro Preto, Campus Morro do Cruzeiro, Ouro Preto, Minas Gerais, Brazil | [4]Instituto de Pesquisas Energéticas e Nucleares IPEN-CNEN, Av. Prof. Lineu Prestes, 2242 – Cidade Universitária, São Paulo, São Paulo, Brazil

Correspondence: Alfredo Antonio Alencar Exposito De Queiroz (alfredo.queiroz@alumni.usp.br)

Received: 31 March 2025 | **Revised:** 2 August 2025 | **Accepted:** 5 August 2025

Funding: The authors acknowledge the Coordination for the Improvement of Higher Education Personnel (CAPES, Process Number: 88887.370250/2019-00), the Brazilian National Council for Scientific and Technological Development (CNPq, Process Number: 316927/2023-6), and the São Paulo Research Foundation (FAPESP, Process Number: 2013/03487-8 and 2024/09091-3) for their financial support and the Multiuser Structural Crystallography Laboratory at the University of São Paulo's São Carlos Physics Institute (LaMuCrEs-IFSC/USP).

Keywords: chondroitin sulfate | organic memristors | Raman spectroscopy | silver nanoparticles | thermal stability

ABSTRACT

Organic memristors (OMEMRs) based on biopolymeric matrices functionalized with silver nanoparticles (AgNPs) are emerging as promising candidates for next-generation non-volatile memory technologies, owing to their multilevel resistive switching behavior, scalability, and compatibility with solution-processable fabrication methods. In this study, AgNPs were coordinated with chondroitin sulfate (ChS) to produce Ag@ChS-based OMEMRs, which were fabricated via spin-coating and subjected to a comprehensive thermal stability assessment using temperature-resolved Raman spectroscopy over the 25°C–275°C range. The Raman spectra revealed a prominent vibrational mode at 76 cm^{-1}, attributed to AgNP lattice dynamics, along with a distinct Ag–O stretching feature near 240 cm^{-1}, indicative of coordination with carboxylate groups within the ChS matrix. A marked attenuation of sulfate-associated Raman bands was observed at approximately 175°C, signifying a critical degradation threshold associated with desulfation, interfacial breakdown, and irreversible loss of memristive functionality. These findings demonstrate that Raman spectroscopy provides a sensitive, non-destructive platform for probing thermally induced molecular transformations and diagnosing early-stage failure in biopolymer-based memristive systems. The insights gained herein offer valuable guidance for the rational design of thermally robust organic memory devices.

1 | Introduction

Modern computing systems remain largely grounded in the von Neumann architecture, first proposed in the mid-20th century as a practical blueprint for general-purpose machines. Characterized by the separation of processing and memory units connected through a shared bus, this design has endured for decades. However, its continued dominance imposes a significant cost, as it inherently limits performance due to the sequential transfer of data and instructions across the bus. With vNA, both storage and processing of data are separated by a bus system, a physical bottleneck via which instructions must be fetched and data must be transferred [1].

The von Neumann bottleneck (vNB) imposes a fundamental limitation on computational throughput, particularly in scenarios involving large-scale data processing and high energy demand [2]. This architectural constraint, arising from the separation between memories and processing units, leads to substantial latency and inefficiencies in data transfer. Consequently, minimizing energy consumption has emerged as one of the foremost challenges in contemporary electronic and computer system design [3].

In 2020, the electricity consumption of the information and communication technology sector, encompassing general purpose technological equipment and data centers, accounted for approximately 4%–6% of the global electricity demand. This figure has escalated concomitantly with the widespread adoption of mobile devices and intelligent systems, notably within the Internet of Things (IoT) ecosystem [4]. Recent advances in green computing focusing on energy efficient, high speed, and high bandwidth information storage and processing have demonstrated significant potential to mitigate the von Neumann bottleneck (vNB) and substantially curtail energy losses attributed to Joule heating.

Multiple strategies have been proposed to mitigate the vNB, including the integration of critical memory within high-speed cache architectures, multithreading for concurrent task management, parallel processing paradigms, and innovative memory bus designs aimed at enhancing bandwidth and reducing latency. Despite these advancements, the ever-increasing demands for computational power, particularly in domains such as big data analytics and scientific computing, continue to challenge the effectiveness of these traditional approaches, underscoring the necessity for more transformative and energy-efficient solutions [5].

A promising strategy to address speed and thermal limitations in electronics lies in architectures that integrate processing and storage within memory elements, reducing data transfer and emulating neural efficiency. Rooted in Chua's memcomputational systems, this approach employs memristors, memcapacitors, and meminductors to unify computation and memory on a single substrate [6]. Among these, memristors exhibit a memory effect by retaining the history of current flow, enabling nonvolatile operation. Their ability to preserve state without continuous power makes them strong candidates to replace traditional DRAM and transistor-based components. This not only reduces energy consumption and heat generation but also addresses core limitations of conventional architectures [6].

The field of memristive devices has progressed markedly since the first TiO_2 thin-film memristor with oxygen vacancies was fabricated by HP Laboratories, catalyzing extensive exploration of inorganic, organic, and hybrid material systems [7]. More recently, organic memristors (OMEMRs) incorporating silver nanoparticles (AgNPs) have garnered attention as low-power, flexible memory platforms, owing to the local electric field enhancement by AgNPs that increases electron trap density and lowers Coulomb barriers, thereby promoting efficient charge transport [8]. Parallel advances in resistive switching have emerged in solid proton-conducting electrolytes within metal–insulator–metal configurations; notable among these are Ag-tetraethylene glycol nanocomposites where resistive dynamics stem from the electrochemical formation and rupture of Ag^+ conductive filaments under applied bias [8]. These developments underscore the versatility of memristive materials and highlight the pivotal role of nanoscale architecture in defining device performance.

Recent advances in organic electronics have highlighted the utility of biopolymers such as silk fibroin and chitosan as sustainable matrices for organic memristive devices due to their favorable ionic transport properties and environmental compatibility [9, 10]. In this context, chondroitin sulfate (ChS), a naturally occurring sulfated glycosaminoglycan, emerges as a promising candidate for the development of OMEMRs. Its intrinsic proton-conducting capability [11], arising from abundant sulfate and carboxylate groups, facilitates efficient ionic migration, a key mechanism underpinning resistive switching phenomena. Moreover, ChS exhibits excellent film-forming properties, biocompatibility, and chemical versatility, which are critical for integrating functional materials such as metal nanoparticles into hybrid memristive architectures. These attributes position ChS as a compelling platform for next-generation bio-organic memory devices operating at low power and under ambient conditions.

Although ChS has been extensively characterized by vibrational spectroscopy [12] and widely utilized as a reducing and stabilizing agent for AgNPs in biomaterial applications [13], its potential for memristive technologies has yet to be fully explored. In particular, no Raman investigations to date have addressed the structural and electronic behavior of OMEMRs fabricated from silver-functionalized ChS (Ag@ChS). Here, we report the fabrication of Ag@ChS OMEMRs via an eco-friendly in situ chemical reduction of Ag^+ ions mediated by the proton-conducting functionalities of ChS.

Given the pronounced temperature dependence of resistive switching mechanisms, temperature-resolved Raman spectroscopy (25°C–275°C) was employed to probe the molecular-scale interactions between Ag/Ag^+ species and the ChS matrix, enabling the identification of vibrational markers associated with coordination dynamics, filament nucleation, and thermal degradation. Raman spectroscopy, with its sensitivity to vibrational modes, phase transitions, and defect states, proved essential for elucidating the structural and electronic signatures governing the device performance and stability. These insights not only highlight the viability of ChS as a sustainable, bio-derived platform for OMEMRs but also demonstrate the critical role of in situ Raman spectroscopy in revealing the structure–property–function relationships under operational and thermal stress, paving the way for rational design and optimization of next-generation organic memory devices.

2 | Experimental

2.1 | Materials

All chemicals and reagents used, namely, chondroitin sulfate sodium salt (lyophilized powder, ^{13}C-NMR Spectrum: ≥ 60%), silver nitrate ($AgNO_3$, purity ≥ 99,0%), and indium tin oxide ($In_2O_3{\cdot}SnO_2$) coated with polyethylene terephthalate film (ITO-PET, surface resistivity: 60 Ω/sq) were purchased from Sigma-Aldrich (São Paulo, SP, Brazil) and used without further purification.

2.2 | Ag@ChS MEMR Device Fabrication and Characterization

Ag@ChS was prepared by mixing $AgNO_3$ (Sigma-Aldrich) 6 mM with 5 mL of a 1 wt.% ChS (chondroitin-6-sulfate, Sigma-Aldrich) solution to form a transparent ChS-$AgNO_3$ mixture one. The ChS-$AgNO_3$ films were deposited on PET-ITO substrates via a spin-coating process at 3000 rpm for 25 s. The spin-coated films were then exposed to photo-irradiation by a UV-LED light (4.5 mW) source at 365 nm for 20 min, and a UV–visible spectrophotometer (Varian, Cary 50, $\lambda = 300–600$ nm) recorded the optical properties of AgNPs. The crystal structure of Ag@ChS was examined by X-ray diffraction (XRD) analysis on a Shimadzu XRD 6000 diffractometer between 30° and 70° and at 1.54 Å wavelength from Cu Kα radiation. The values set for XRD diffractometer operation were 40 kV/30 mA. A Zetasizer Nano series Malvern instrument Nano Zs characterized the colloidal stability of the Ag@ChS solution and the hydrodynamic size of Ag nanoparticles.

The fabricated Ag@ChS OMEMRs were electrically characterized by a programmable electrometer (Keithley 2612) at 25°C according to the standard two-point method. Measurements were performed applying a voltage ranging between a positive value and a negative one with a 100-mV scan step and a 10-μA set current compliance, adopting three cycles of the I/V characteristic curves. All electrical characterizations were performed at room temperature (25°C).

2.3 | Raman Measurements

A Horiba LabRAM HR Evolution Jobin Yvon Raman spectrometer equipped with a liquid-nitrogen-cooled CCD detector and coupled with a 600-g/mm grating confocal Olympus microscope (BX41) was used for Raman spectroscopy. The laser beam was focused precisely using a ×50 Olympus microscope objective, with a 633-nm excitation wavelength for the experiments. The power of the laser used for the Raman excitation of the samples was 0.94 mW for obtaining a viable signal-to-noise ratio, and the spectral resolution was 1 cm^{-1}. A peak at 520.7 cm^{-1} from a silicon standard wafer was used as a reference for the spectra calibration.

High-temperature Raman spectroscopy measurements were carried out using a Linkam CCR1000 heating stage coupled with a T95 temperature controller. Ag@ChS samples were deposited onto standard glass microscope slides and mounted within the heating stage, which allows precise thermal control from ambient temperature (25°C) up to 250°C, with a constant heating rate of 1°C min^{-1}. Raman spectra were recorded at selected isothermal points between 25°C and 250°C, primarily at 25°C intervals, including 175°C, to monitor spectral changes associated with a thermally induced transition observed in preliminary analyses.

3 | Results and Discussion

3.1 | Nanostructural and Plasmonic Properties of Ag@ChS OMEMRs

The integration of noble metal nanoparticles into biopolymeric matrices has garnered significant interest due to the resulting enhancement in optical, electronic, and physicochemical properties, which are highly relevant for applications in plasmonic sensing, memristive devices, and bioelectronics. In this context, ChS, a sulfated glycosaminoglycan, serves not only as a stabilizing and reducing agent but also as a functional platform for the incorporation of AgNPs, yielding hybrid nanostructures with tunable optoelectronic behavior. The structural and optical characteristics of these Ag@ChS nanocomposites were investigated using UV–Vis spectroscopy, providing insights into AgNPs dispersion, surface plasmon resonance (SPR) phenomena, and electronic band structure.

The presence of a well-defined SPR band centered at 418 nm in the UV–Vis absorption spectrum (Figure S1a) confirms the successful formation of Ag@ChS nanostructures. The relatively narrow full width at half maximum (FWHM) of around 80 nm suggests high monodispersity and uniformity in nanoparticle size distribution, consistent with literature reports on silver–chitosan hybrids exhibiting SPR bands in the 410- to 430-nm range [14]. Tauc plot analysis of the absorption data revealed an optical bandgap of approximately 2.71 eV (Figure S1b), in agreement with values observed for plasmonically active biopolymer-based nanocomposites [15].

The SPR peak near 410 nm, coupled with the FWHM, indicates strong plasmon–exciton interactions and enhanced visible-light absorption. This optical behavior underscores the effective stabilization provided by the ChS matrix and the suppression of AgNPs aggregation. Notably, this bandgap is slightly lower than that reported for analogous starch-based memristive systems incorporating graphene quantum dots (2.84 eV) [16], illustrating the tunability of optoelectronic properties in organic–inorganic hybrid devices.

The XRD pattern of the Ag@ChS (Figure S2) reveals distinct diffraction peaks at 2θ values of 33°, 38°, 55°, and 66°, corresponding to the (111), (200), (220), and (311) crystallographic planes of face-centered cubic (FCC) Ag, in agreement with JCPDS Card No. 04–0783. These results confirm the formation of crystalline Ag nanoparticles within the ChS matrix. The average crystallite size of the Ag phase was estimated using the Scherrer equation [17]:

$$\tau = \frac{K \cdot \lambda}{\beta \cdot \cos\theta} \quad (1)$$

where τ denotes the mean crystallite dimension, K is the shape factor (0.94), λ is the Cu-Kα radiation wavelength (0.15406 nm), β is the FWHM of the (111) reflection, and θ is the Bragg angle.

XRD analysis revealed that the AgNPs embedded within the biopolymeric matrix of the Ag@ChS-based OMEMRs device exhibit an average crystallite size of approximately 70 nm, as estimated via the Scherrer equation. This nanoscale dimension confirms the effective formation and uniform distribution of Ag nanodomains within the ChS framework. Comparable particle sizes have been successfully employed in memristive systems, such as the atomic bridge memristor based on Ag and two-dimensional GeSe [18], which utilized AgNPs of approximately 80 nm in diameter. This alignment reinforces the structural relevance of the particle size obtained in the present study and underscores the methodological reliability of the crystallite size estimation. Together, these findings highlight the structural integrity and application potential of the Ag@ChS for bioinspired resistive switching devices.

A colloidal stability of AgNPs within the ChS solution, as measured by a zeta potential (ζ) of −31 mV (Figure S3), indicates substantial electrostatic repulsion and uniform dispersion, an essential requirement for consistent spin-coating onto PET–ITO substrates. According to classical DLVO theory, colloidal stabilization arises from the delicate balance between van der Waals attraction and ζ-dependent electrostatic repulsion, with absolute ζ values exceeding around 30 mV typically denoting stability against aggregation [19]. Recent critical analyses further reinforce that ζ measurements must account for ionic strength and surface conductivity effects to yield reliable predictions of colloidal behavior, especially in nanoparticle systems [20]. The observed $\zeta = -31$ mV thus confirms a DLVO-predicted energy barrier sufficient to suppress agglomeration within the ChS matrix, ensuring uniform AgNPs coverage and preserving the functional integrity of the OMEMRs device.

3.2 | Resistive Switching Dynamics and Thermal Effects

Figure S4a shows the typical memory characteristics of the Ag@ChS OMEMRs device, where high-resistance state (R_{OFF}) to low-resistance one (R_{ON}) can be observed. The I–V curve labeled S4a exhibits a non-pinched hysteresis, as the forward and reverse sweeps do not intersect at the origin ($I[V = 0] \neq 0$), violating the strict definition of first-order memristors [21]. This behavior indicates internal complexity consistent with multi-state memory and coupled nonlinear dynamics typical of advanced organic or hybrid memristive devices [22]. The data were modeled by voltage-dependent asymmetric functions for each sweep direction, introducing path dependence without explicit dynamic variables, indicative of a second-order memristive system governed by coupled state variables representing electronic conduction and dipolar polarization [23].

The I–V characteristics in Figure S4a were modeled using distinct voltage-dependent current expressions for each sweep direction [24]:

$$I(V, d) = a_d \tanh(bV) + c_d V^3 - d_d e^{-e_d|V|} \tag{2}$$

Here, the coefficients a_d,c_d,d_d, and e_d vary with the sweep direction $d \in \{forward, backward\}$, introducing explicit path dependence without invoking dynamic state variables. This asymmetry, however, gives rise to an implicit memory effect, characteristic of second-order memristive behavior. From a phenomenological standpoint, Ag@ChS OMEMRs conform to the formalism of second-order memristors, governed by [25]:

$$I(t) = G\big(w_1(t), w_2(t)\big).\, V(t),\ \frac{dw_1}{dt} = f_1\big(V, w_1\big),\ \frac{dw_2}{dt} = f_2\big(V, w_2\big) \tag{3}$$

where $w_1(t)$ and $w_2(t)$ represent coupled internal processes, typically linked to mechanisms such as electronic conduction and dipolar polarization.

Numerical fitting of Equations (2) and (3) to the experimental data yielded coefficients of determination $R^2 = 0.952$ (forward) and 0.948 (reverse), indicating an excellent match to second-order memristive dynamics. The fitted expressions are as follows:

Forward sweep:

$$I(V) = \left| -1.0.10^{-3}.\tanh(4V) - 1.0.10^{-4}V^3 + 2.0.10^{-5}.\, e^{-20|V|} \right| \tag{4}$$

Backward sweep:

$$I(V) = \left| -1.2.10^{-3}.\tanh(4V) - 1.5.10^{-4}V^3 + 3.0.10^{-5}.\, e^{-18|V|} \right| \tag{5}$$

The voltage-dependent I–V profiles exhibit directional asymmetry, indicative of second-order memristive behavior governed by coupled internal states. Such behavior aligns with models where nonlinear electronic transport and ion migration or dipolar effects give rise to memory [24].

At ±1.5 V, ON/OFF ratios exceed two orders of magnitude, evidencing strong nonlinearity and resistive switching. These features are attributed to the electromigration of Ag and Ag^+ within the ChS matrix, which modulates the nucleation and dissolution of conductive filaments. The coordination of Ag^+ with oxygen-containing functional groups in the ChS, particularly carboxylate ($-COO^-$) and sulfate ($-SO_3^-$) moieties, plays a critical role in modulating Ag^+ mobility and consequently restricting uncontrolled filament overgrowth. These groups act as electrostatic anchoring sites, forming stable Ag–O coordination complexes that localize Ag^+ distribution and guide filament formation along energetically favorable, self-limiting paths [26].

Such coordination suppresses excessive filament growth, enhances switching uniformity, and stabilizes resistive states. Prior studies on diffusive memristors have demonstrated that these ligand–metal interactions are essential for confining filament expansion and promoting reliable resistive switching behavior in hybrid organic systems. Therefore, the observed second-order memristive behavior in the Ag@ChS devices emerges as a direct consequence of these coordinated ionic and structural dynamics, validating the critical correlation between molecular-level interactions and macroscopic device performance. Electrochemical impedance spectroscopy further supports the presence of ionic–electronic coupling and diffusion-driven switching dynamics, characteristic of diffusive memristors with nonvolatile retention properties [26].

Temperature significantly affects the I–V characteristics of Ag@ChS OMEMRs by modulating charge transport and resistive switching (Figure S5). Increased temperatures enhance carrier mobility and alter interfacial barriers, reducing the high resistance state, while promoting Ag^+ and oxygen vacancy diffusion that governs filament dynamics. Above around 175°C, Raman spectral changes indicate a phase transition that coincides with a sharp drop in conductivity and compromised device performance (Figure S5) [27]. These thermally driven structural and electrical effects highlight the limitations of conventional transport models such as space charge limited current, Poole-Frenkel emission, and variable range hopping. To more accurately describe the observed behavior, a hybrid conduction model was employed, integrating

Arrhenius-type thermally activated transport with hopping conduction mechanisms [28]:

$$I(V,T) = \frac{I_o \exp\left(-\frac{E_a^{eff}}{k_B T}\right)}{1+\exp\left(\alpha\left(T-T_c\right)\right)} + A\exp\left(\frac{-B}{T}\right) + I_{res} \tag{6}$$

where I_o is the pre-exponential factor, E_a^{eff} is the effective activation energy, α the thermal transition parameter, A and B are constants characterizing the hopping conduction term, and I_{res} accounts for temperature independent leakage current.

Figure S6 shows the 3D surface plot of I(V,T) from Equation (6), revealing a nonlinear dependence on temperature and voltage, with hopping conduction dominating at lower temperatures and a sharp transition to Arrhenius-type behavior near Tc. This dual-regime conduction, commonly observed in disordered organic semiconductors [29], highlights the complex interplay between thermal and electric stimuli in Ag@ChS OMEMRs. Understanding this thermally induced transport switching is crucial for optimizing device performance under variable thermal conditions, especially in applications demanding thermal stability and switching reliability.

Figure S7 depicts the temperature-dependent modulation of the resistance ratio $R_{\mathrm{OFF}}/R_{\mathrm{ON}}$ in Ag@ChS OMEMRs during forward and backward voltage sweeps. The forward sweep reveals an exponential decline from approximately 292°C at 25°C, attributable to thermally activated carrier transport and progressive filament destabilization. In contrast, the backward sweep exhibits a sigmoidal increase commencing near 21, indicative of enhanced resistive contrast mediated by field-driven ionic migration and dipolar reorientation. The convergence of these curves near 164°C signifies a transition in the prevailing switching mechanisms. This pronounced directional asymmetry reflects the interplay of coupled internal state variables and intrinsic path dependence, hallmark features of second-order memristive systems. These insights are essential for correlating thermal effects with molecular and structural dynamics, thereby informing strategies for device optimization under variable thermal regimes.

The long-term retention stability of Ag@ChS OMEMRs was evaluated over 100 h by monitoring two key metrics that quantify resistance drift and stochastic fluctuations, namely the retention deviation index (RDI) and the normalized retention noise (σ_{norm}). These parameters collectively provide a rigorous framework for assessing the temporal stability and operational reliability of memristive behavior in organic hybrid architectures. The RDI represents the average relative deviation from the initial resistance R_0 and is defined as [30, 31]:

$$RDI = \frac{1}{N}\sum_{i=1}^{N}\left(\frac{R\left(t_i\right)-\left(R_0\right)}{R(0)}\right).100 \tag{7}$$

where $R\left(t_i\right)$ denotes the resistance at time t_i, R_0 is the initial resistance value, and N is the total number of samples.

The normalized retention noise σ_{norm}, which quantifies resistance fluctuations relative to the mean, is given by [32]:

$$\sigma_{norm} = \frac{1}{\bar{R}}\sqrt{\frac{1}{N}\sum_{i=1}^{N}\left(R\left(t_i\right)-\bar{R}\right)^2} \tag{8}$$

where $\bar{R}$ representing the average resistance over the measurement interval.

Figure S8 illustrates the retention performance of Ag@ChS OMEMRs over a 100-h period, with retention metrics reflecting both promising behavior and consistency with organic electronic systems. Under forward sweep, the RDI reached 8.04% for the low resistance state ($\mathrm{R_{ON}}$) and 1.28% for the high resistance state (R_{OFF}), with corresponding normalized noise (σ_{norm}) values of 0.05 and 0.01, respectively. These results indicate moderate variability in the conductive state, likely due to reversible silver filament formation, and high stability in the insulating regime [33]. In contrast, backward sweep measurements yielded improved RDIs of 5.59% (R_{ON}) and 3.84% (R_{OFF}), with σ_{norm} values of 0.04 and 0.05. This enhanced stability under reverse bias may arise from relaxation dynamics or reorganization of charge trapping and ionic domains within the ChS matrix [34].

The pronounced asymmetry observed between forward and backward voltage sweeps reflects resistive switching mechanisms governed by field-driven ionic migration and interfacial asymmetries at the electrode interfaces [35]. From a technological perspective, these characteristics highlight the potential of Ag@ChS devices for applications in low-power non-volatile memory storage, neuromorphic computing systems, and biocompatible sensor arrays, where moderate variability in the low resistance state (R_{ON}) is tolerable, while stability in the high resistance state (R_{OFF}) remains critical. Continued optimization efforts focusing on device encapsulation, uniformity of nanoparticle dispersion, and regulation of ionic mobility through material design are expected to further reduce electrical noise and enhance resistance state retention over prolonged operational periods.

The radar plot in Figure S9 provides a normalized comparison of three key performance metrics, namely, ON/OFF ratio, retention time, and operating voltage, for the Ag@ChS device and memristive devices reported in references [9, 10]. The Ag@ChS device exhibits a balanced performance profile, combining moderate ON/OFF ratio (~0.2 normalized), excellent retention (normalized to 1.0), and moderate operating voltage (~0.75). In contrast, the literature devices show either higher ON/OFF ratios (up to 1.0) but very poor retention (~0.03), or require higher operating voltages. This comparison highlights the Ag@ChS device's suitability for applications demanding long-term data retention and energy-efficient operation, making it a promising candidate for stable non-volatile memory.

3.3 | Raman Analysis of Thermally Induced Structural Changes

Figure 1a illustrates the molecular mechanism underlying the formation of AgNPs mediated by ChS. Initially, $\mathrm{Ag^+}$ interact with functional groups present in the ChS matrix, notably carboxylate

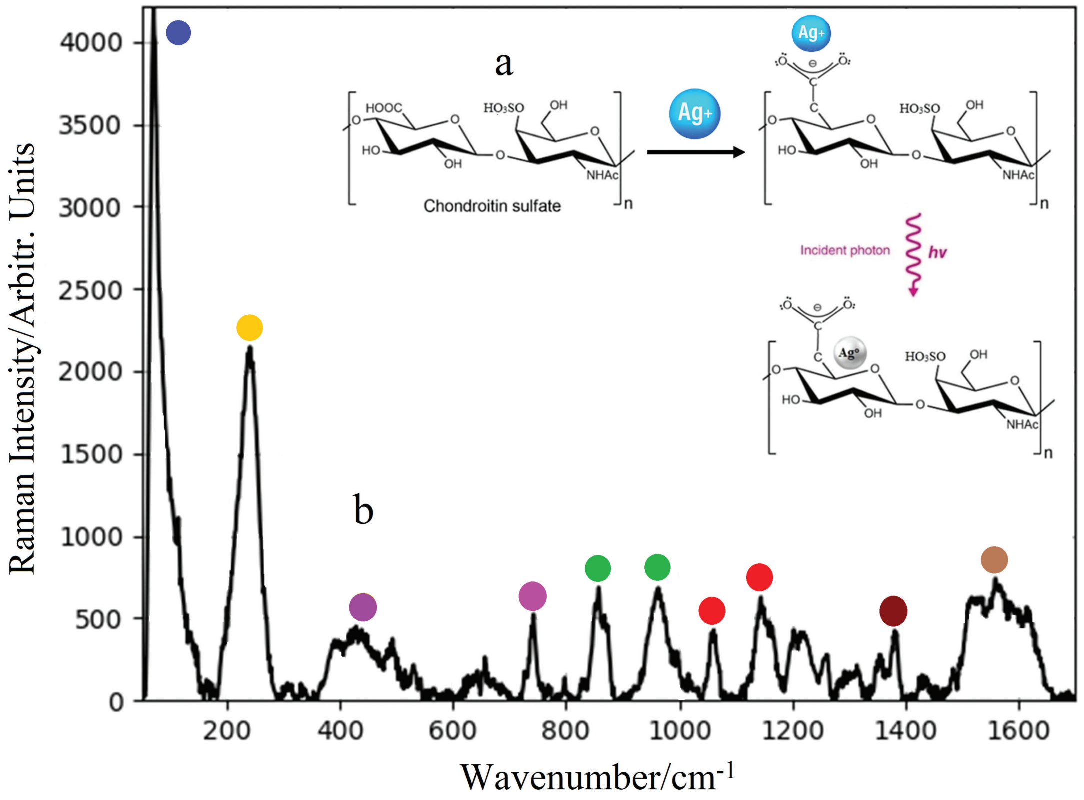

FIGURE 1 | (a) Schematic illustration of the in situ photochemical synthesis of Ag nanoparticles within the chondroitin sulfate (ChS) matrix, showing Ag^+ coordination to $–COO^−$ and $–SO_3^−$ groups followed by photoreduction to metallic Ag^0. (b) Room temperature (25°C) Raman spectrum of Ag@ChS, highlighting key vibrational modes. Symbols indicate the spectral contributions of specific functional groups: (🔵) surface acoustic vibrations of Ag nanoparticles (~70 $cm^{−1}$) linked to plasmon–phonon coupling and SERS enhancement, (🟡) Ag–O/Ag^+ coordination modes (~220 $cm^{−1}$), (🟣) glycosidic and carboxylate-related deformation modes (~400 $cm^{−1}$), (🟣) symmetric deformation of $OSO_3^−$ groups (~780 $cm^{−1}$), (🔴) $OSO_3^−$ symmetric/asymmetric stretching modes (~1076–1150 $cm^{−1}$), (🔴) N-acetyl group ($NHCOCH_3$) deformation (~1370 $cm^{−1}$), (🟢) C–O and C–C backbone vibrations (~850–950 $cm^{−1}$), and (🟤) Amide I band (~1600 $cm^{−1}$), all enhanced by AgNP coordination.

($–COO^−$) and sulfate ($–SO_3^−$) moieties, leading to the formation of a coordination complex. This interaction is facilitated by the electron-donating capacity of oxygen atoms in these groups, which stabilize Ag^+ through electrostatic and coordination bonding. Upon exposure to incident photons (hν), a photoreduction process is triggered wherein the coordinated Ag^+ undergo a redox transformation, resulting in the nucleation and growth of metallic silver nanoparticles (Ag^0) directly on the polymeric matrix. This process effectively anchors the nanoparticles to the chondroitin sulfate chains, promoting localized SPR (LSPR) phenomena and enhancing the system's optical and Raman-active properties.

The Raman spectrum presented in Figure 1b corresponds to chondroitin sulfate (ChS) functionalized with AgNPs. A prominent band at ~220 $cm^{−1}$ is assigned to a T'Ag^+ vibrational mode, associated with Ag^+ interactions with oxygen-donating groups such as carboxylate ($–COO^−$) and sulfonate ($–SO_3^−$) embedded within the polysaccharide matrix [36]. It is well established that typical T'Ag lattice modes lie within the low-frequency regime, generally between 20 and 100 $cm^{−1}$. For instance, Colomban and Lucazeau [37] reported a strong Ag^+ lattice mode near 20 $cm^{−1}$ in stoichiometric β-alumina, along with weaker satellite bands at 23 and 27 $cm^{−1}$, attributed to intraplane vibrational coupling at 20 K. These sharp features are characteristic of highly ordered crystalline environments with well-defined interstitial sites.

In contrast, the observed upshift of the Ag-related band to ~220 $cm^{−1}$ in Ag@ChS can be attributed to the disordered and spatially confined coordination environment of the polymer matrix. First-principles calculations by Liu and Jiang [36] indicate that, in systems with restricted geometries or increased local rigidity, conditions satisfied within the dense ChS network, Ag^+ vibrational modes can shift markedly to higher wavenumbers, even above 200 $cm^{−1}$.

Furthermore, experimental studies of Ag^+ complexes with rigid or planar oxygen-donating ligands, such as carboxyl and carbonyl groups, report characteristic Raman shifts in the 220- to 240-$cm^{−1}$ range, attributed to Ag–O stretching modes [38]. Such coordination geometries alter local symmetry and bonding strength, enhancing both the energy and Raman activity of Ag–ligand vibrations, particularly those with A_{1g} or B_{1g} symmetry. In Ag@ChS, the coordination environment is consistent with pseudo-planar or pseudo-linear geometries, as inferred from the Raman signature and supported by the rich presence of multidentate ligands. Taken together, these considerations support the assignment of the 220-$cm^{−1}$ band not as a bulk-like T'Ag lattice mode, but as a localized Ag^+–ligand symmetric stretching vibration, modified by coordination-induced rigidity and spatial confinement.

This interpretation is further corroborated by the presence of a distinct, lower-wavenumber band at ~70 cm^{-1}, which is attributed to surface acoustic or lattice vibrational modes of AgNPs, typically observed in the 20- to 100-cm^{-1} range [39, 40]. Therefore, this analysis distinguishes between bulk-like phonon modes and coordination-specific vibrations, with the 220-cm^{-1} band aligning with previously reported shifts associated with constrained coordination environments [36, 38].

The contrast between the vibrational behavior observed in the ChS matrix and that of β-alumina further underscores the role of the local environment in modulating Ag^+ dynamics. In β-alumina, Ag^+ resides in structurally well-defined interstitial sites with crystalline symmetry (e.g., C_{2v} or D_{3h}), where lattice phonon modes remain restricted to the low-frequency regime due to strong periodicity and long-range order [37]. Conversely, the ChS matrix is highly flexible, amorphous, and chemically heterogeneous, offering a distribution of dynamic coordination sites where Ag^+ can adopt distorted geometries with reduced symmetry. These factors promote stronger Ag–O interactions, increased force constants, and a shift of the corresponding vibrational modes to significantly higher wavenumbers. This behavior is consistent with previous observations in soft coordination environments and highlights the sensitivity of Ag^+ vibrational modes to structural disorder and local electronic density. The presence of multidentate ligands and spatial confinement within the biopolymer matrix effectively mimics a rigid coordination pocket, enabling the emergence of localized high-frequency Ag–ligand modes absent in more ordered crystalline hosts.

Importantly, these Ag–ligand coordination interactions have profound implications for the functional behavior of Ag@ChS in memristive applications. The coordination of Ag^+ with oxygen-rich groups not only stabilizes silver nanoparticles but also critically influences conductive filament growth, a key mechanism in diffusive resistive switching. Previous work shows that Ag–O coordination imparts electrostatic and steric constraints that limit Ag^+ mobility and prevent uncontrolled filament formation. For instance, Krishnan et al. [27] demonstrated that ligand-mediated energy barriers in polymer electrolytes confine Ag^+ migration and localize filament nucleation.

Complementarily, Dirkmann et al. [41] used kinetic simulations to reveal that the geometry and bond strength of Ag–O interactions control filament morphology, including its diameter and propagation speed, thereby promoting self-limiting and uniform conductive pathways. Supporting this concept, Zhao et al. [42] demonstrated that acidic polysaccharide matrices can spatially confine Ag^+ ions within polar functional environments, resulting in discrete conductive filaments exhibiting quantized conductance and high endurance. Although their study focuses on device-level behavior, it highlights the pivotal role of ionic coordination in guiding filament dynamics.

In the Ag@ChS hybrid investigated here, the dense network of carboxylate and sulfonate groups forms a multisite chelation environment that immobilizes Ag^+, fostering reversible Ag^+/Ag^0 redox transitions and spatial confinement of conductive channels. These coordination-mediated effects are essential for achieving stable, uniform, and nonvolatile resistive switching and are consistent with the observed Raman signatures of Ag–ligand bonding. These coordination effects are further evidenced by distinct vibrational features in the Raman spectra, which reflect Ag^+–ligand interactions and structural rearrangements within the ChS matrix. The intense band at ~220 cm^{-1} corresponds to symmetric Ag^+–ligand stretching vibrations, consistent with Raman-active modes (e.g., A_1g or B_1g) typical of linear or quasi-planar coordination environments such as those described by D_2h or C_2v symmetries. These coordination geometries enhance Raman activity through modulation of the molecular polarizability. In addition, a low-wavenumber feature below 100 cm^{-1} (~70 cm^{-1}) is assigned to lattice or surface acoustic vibrations of AgNPs, commonly exhibiting Ag or Eg symmetry under near-spherical conditions, and activated through quantum confinement and SERS effects [36, 38–40].

The weak-to-moderate Raman band observed near ~780 cm^{-1} (Figure 1b) is assigned to the symmetric bending (δs) of O–S–O in the sulfate groups of chondroitin sulfate (ChS). Raman microspectroscopy studies have consistently shown that sulfated glycosaminoglycans (GAGs), including ChS, exhibit diagnostic vibrational signatures in the 730- to 860-cm^{-1} region, corresponding to axial and equatorial C–O–S stretching as well as O–S–O deformation modes [43]. In the higher-frequency spectral region between 1000 and 1500 cm^{-1}, multiple modes are evident and can be assigned to C–C stretching, C–O bending, symmetric SO_3^- stretching vibrations (typically near ~1065 cm^{-1}), and N-acetyl functional group modes. These vibrational features are notably enhanced under surface-enhanced Raman scattering (SERS) conditions, particularly in the presence of noble metal nanoparticles such as AuNPs, which generate intense localized SPRs that amplify the Raman response of functional groups within GAG matrices [44].

Coordination of ChS with silver nanoparticles (AgNPs) further induces detectable spectral modulations in both frequency and intensity, reflecting local structural reorganizations and strong electronic coupling between the sulfate and carboxylate moieties of the polysaccharide and the metal surface. These observations are consistent with previous SERS investigations involving ChS–nanoparticle complexes, where similar vibrational perturbations were attributed to chelation-driven symmetry alterations and polarizability changes at the metal–ligand interface [45].

Temperature-dependent Raman spectra of Ag@ChS OMEMRs (Figures 2 and 3) reveal pronounced thermally induced changes in vibrational intensity and FWHM, indicative of structural reorganization and coordination dynamics at the biopolymer–nanoparticle interface. The irreversibility of these thermal effects was thoroughly evaluated. As shown in Figure 2a, above 175°C, the characteristic Raman bands of the material disappear and are replaced by a broad fluorescence background, a clear signature of thermal degradation. This behavior confirms that the structural and chemical transformations occurring beyond this threshold are irreversible. Consequently, Raman measurements during the cooling cycle were deemed unnecessary, as the material no longer recovers its original spectroscopic features after thermal exposure, further supporting the conclusion of irreversible degradation.

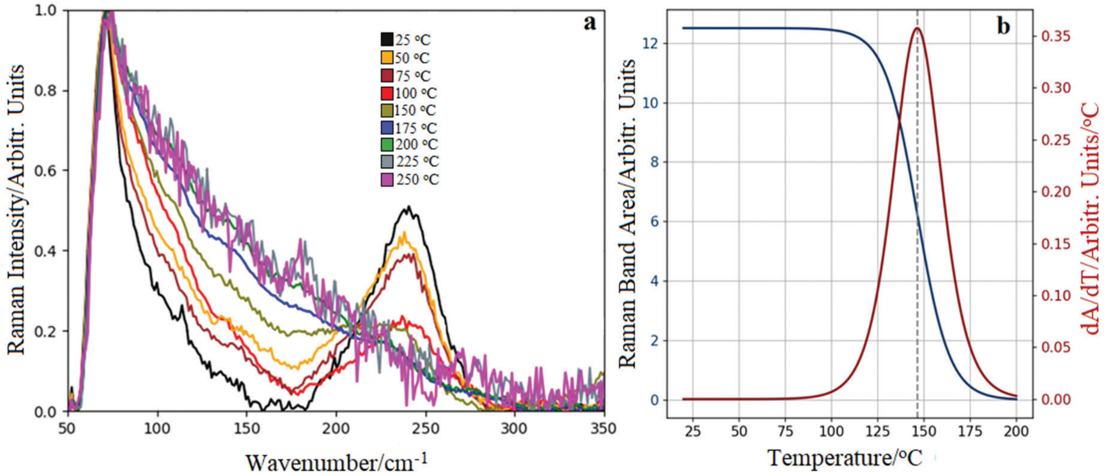

FIGURE 2 | Temperature-dependent Raman response of Ag@ChS OMEMRs. (a) Evolution of Raman spectra recorded from 50 to 350 cm^{-1} using a 532-nm laser at 1% power (15 mW), highlighting vibrational changes in the sulfate-associated mode (~240 cm^{-1}) with increasing temperature. (b) Temperature dependence of the sulfate Raman band area (A) in AgNP@ChS. The primary *y*-axis (blue curve) shows a logistic decay fit representing thermally activated degradation, while the secondary *y*-axis (brown curve) shows its analytical derivative, emphasizing the critical transition region near 150°C. The inflection point (Tc ≈ 150°C) marks the onset of irreversible disruption of Ag–ChS coordination disruption in the hybrid material.

Notably, the $-SO_3^-$-associated mode near 240 cm^{-1} remains spectrally stable up to approximately 150°C, with less than 10% variation in FWHM (Figure 2b), but undergoes abrupt narrowing above this threshold, disappearing completely at 175°C. This spectroscopic transition reflects a thermally activated degradation mechanism, quantitatively described by a sigmoidal exponential decay model [46]:

$$\frac{d}{dT}FWHM(T)=\frac{F_o}{\delta_T}\cdot\frac{e^{-(T-T_c)/\delta_T}}{\left(1+e^{-(T-T_c)/\delta_T}\right)^2} \qquad (9)$$

where $FWHM(T)$ is the vibrational linewidth at temperature T, F_o is the baseline linewidth, T_c the critical transition temperature, and δ_T characterizes the thermal transition width. This model elucidates a narrow thermal destabilization window governing vibrational collapse, correlating spectroscopically with the functional degradation of memristive performance.

Figure 2b presents a graphical analysis of the thermal evolution of the $-SO_3^-$ band area in Ag@ChS OMEMRs, modeled via Equation (9) and its temperature derivative. The sigmoidal decay profile reveals a thermally activated degradation, with the vibrational mode remaining stable up to approximately 150°C and undergoing an abrupt intensity loss beyond the critical temperature (Tc ≈ 151.3°C), reflecting disruption of Ag–O/Ag–S coordination. The derivative curve sharply defines a narrow thermal window (ΔT ≈ 10°C–15°C), underscoring the rapidity and quasi-irreversible nature of the structural collapse. These quantitative insights into vibrational band attenuation delineate fundamental constraints on the thermal resilience of Ag@ChS-based OMEMRs, with direct implications for their deployment in memory applications under thermally variable conditions.

Figure 3 shows temperature-dependent Raman spectra (1000–2000 cm^{-1}) of Ag@ChS OMEMRs, revealing progressive attenuation and complete loss of $-SO_3^-$ and $-COO^-$-associated bands (e.g., 1063–1600 cm^{-1}) at 175°C. This spectral collapse indicates thermally driven desulfation and cleavage of sulfate ester bonds, disrupting AgNPs coordination [43]. The consequent loss of ion–dipole interactions and interfacial order promotes AgNPs aggregation and suppresses filament formation. Concurrently, elevated temperatures enhance phonon–phonon scattering and disorder, reducing Raman cross-sections and masking vibrational features [47]. These irreversible changes correlate with functional degradation of the Ag@ChS OMEMRs device, as the supramolecular framework required for ionic transport and charge retention destabilizes under thermal stress.

Figures 2 and 3 show that thermal exposure above 175°C induces irreversible transformations in Ag@ChS OMEMRs, including desulfation, polymer backbone disruption, and interfacial breakdown, culminating in structural and electronic degradation. These results emphasize the importance of thermal control in memristive devices and validate temperature-resolved Raman spectroscopy as a sensitive probe of stress-induced changes. To model the thermal evolution of vibrational features, the integrated intensities of the 1600 cm^{-1} (Amide I) and 1150 cm^{-1} ($-SO_3^-$) bands were fitted using a Boltzmann-type sigmoidal function [48]:

$$A(T)=\frac{A_o}{1+e^{\left(\frac{T-T_c}{\Delta T}\right)}} \qquad (10)$$

where $A(T)$ is the band area at temperature T, A_o the low-temperature baseline, T_c the inflection point of degradation, and ΔT the thermal cooperativity width.

The fitted curves (Figures S10 and S11), accompanied by ±1σ uncertainty envelopes, capture the nonlinear attenuation behavior; reflecting the cooperative nature of thermally activated molecular rearrangements, bond cleavage, and loss of vibrational coherence in the hybrid matrix.

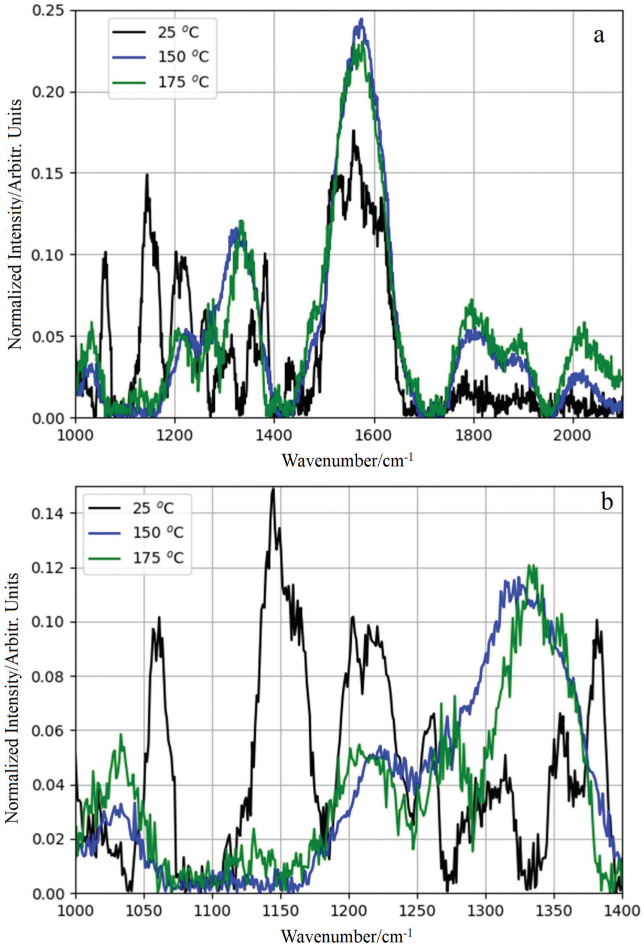

FIGURE 3 | Temperature-dependent Raman spectra of Ag@ChS OMEMRs recorded under air at 25°C, 150°C, and 175°C using a 532-nm laser (15 mW). (a) Spectra (1000–2060 cm^{-1}) highlight attenuation of sulfate (SO_3^-, ~1063 cm^{-1}) and carboxylate (COO^-, 1400–1600 cm^{-1}) bands. (b) Zoomed-in region (1000–1400 cm^{-1}) emphasizes the progressive loss of these bands with heating. Complete collapse at 175°C indicates desulfation, ester bond cleavage, and AgNPs coordination disruption, correlating with functional degradation of the supramolecular memristive framework.

The temperature-induced decay of the 1600 cm^{-1} (Amide I) and 1150 cm^{-1} ($-SO_3^-$ symmetric stretch) Raman bands (Figures S9 and S10) reveals progressive degradation of the Ag@ChS matrix, marked by disruption of hydrogen bonding networks and thermally driven desulfation processes. These transformations compromise the dielectric stability and coordination environment necessary for effective filament formation and charge transport. Sigmoidal fitting of the band area evolution, modeled by Equation (10), yields critical inflection temperatures near 175°C, with a narrow transition width ($\Delta T \approx 18.7°C \pm 2.9°C$) derived from the first derivative. This sharp thermal window suggests a cooperative structural transition involving polymer chain disordering, interfacial softening, and AgNPs redistribution. The observed exponential attenuation of Raman intensity serves as both a molecular-level indicator of irreversible structural collapse and a predictive spectroscopic marker of memristive performance loss under thermal stress.

4 | Conclusions

Ag@ChS OMEMRs devices were successfully synthesized via in situ chemical reduction of silver ions within a ChS matrix, as corroborated by UV–Vis spectroscopy and XRD analyses that confirmed the presence of plasmonically active, crystalline AgNPs. Temperature-resolved Raman spectroscopy provided a detailed molecular-level insight into the structural dynamics governing Ag@ChS OMEMRs stability. The $-SO_3^-$- and $-COO^-$-associated vibrational modes exhibited sigmoidal intensity attenuation above ~175°C, which is indicative of thermally induced desulfation, cleavage of sulfate ester linkages, biopolymer backbone degradation, and disruption of Ag–ChS interfacial coordination. These spectral modifications define a critical thermal threshold, beyond which the functional integrity of the Ag–ChS coordination network collapses, resulting in irreversible degradation of memristive performance.

The high sensitivity and noninvasive character of Raman spectroscopy enabled precise monitoring of these thermally driven structural transitions, validating its application as a diagnostic tool for probing the thermal resilience of hybrid organic–inorganic memristive systems. The sigmoidal decay kinetics and narrow thermal transition windows derived from vibrational linewidth and intensity analyses quantitatively delineate the cooperative nature of molecular disintegration processes affecting device functionality. This vibrational spectroscopic approach thus provides a rapid, cost-effective means to evaluate and predict performance-limiting structural transformations in Ag@ChS-based OMEMRs, facilitating the design of thermally robust memristive architectures for next-generation bioinspired memory and sensing technologies. Future work may include evaluating alternative top electrode materials (e.g., Au and Pt) to further clarify the contribution of interfacial effects and to assess the role of filamentary conduction mechanisms in the observed switching behavior.

Author Contributions

Alfredo Antonio Alencar Exposito De Queiroz and Marcelo Barbosa de Andrade contributed to the Raman measurements and spectral analysis. Alvaro Antonio Alencar de Queiroz was responsible for the preparation of the Ag@ChS MEM device, its electrical measurements, and physicochemical analysis. All authors discussed the results and contributed to the final manuscript.

Acknowledgments

The authors acknowledge the Coordination for the Improvement of Higher Education Personnel (CAPES, Process Number: 88887.370250/2019-00), the Brazilian National Council for Scientific and Technological Development (CNPq, Process Number: 316927/2023-6), and the São Paulo Research Foundation (FAPESP, Process Number: 2013/03487-8 and 2024/09091-3) for their financial support and the Multiuser Structural Crystallography Laboratory at the University of São Paulo's São Carlos Physics Institute (LaMuCrEs-IFSC/USP).

Conflicts of Interest

The authors declare no conflicts of interest.

Data Availability Statement

Data are available from the corresponding author upon reasonable request.

References

1. K. Mambu, H.-P. Charles, M. Kooli, and J. Dumas, “Towards Integration of a Dedicated Memory Controller and Its Instruction Set to Improve Performance of Systems Containing Computational SRAM,” *Journal of Low Power Electronics and Applications* 12, no. 1 (2022): 1–11, https://doi.org/10.3390/jlpea12010018.

2. X. Meng, R. Gao, X. Zhu, and R.-W. Li, “Ion-Modulation Optoelectronic Neuromorphic Devices: Mechanisms, Characteristics, and Applications,” *Journal of Semiconductors* 46, no. 2 (2025): 021402, https://doi.org/10.1088/1674-4926/24100025.

3. E. Gelenbe, “Minimizing Delay and Power Consumption at the Edge,” *Sensors (Basel)* 25, no. 2 (2025): 502, https://doi.org/10.3390/s25020502.

4. N. K. Narang, “Mentor's Musings on Green Challenges for IOT, Edge Computing & All Other Disruptive Digital Technologies,” *IEEE Internet of Things* 8, no. 3 (2025): 4–10, https://doi.org/10.1109/MIOT.2025.10980615.

5. H. Liu and J. Zhai, “Carbon Emission Modeling for High-Performance Computing-Based AI in New Power Systems With Large-Scale Renewable Energy Integration,” *PRO* 13, no. 2 (2025): 1–20, https://doi.org/10.3390/pr13020595.

6. Q. Tian, X. Shan, J. Bian, et al., “Metal Oxide Based Resistive Switching Memristor for Neuromorphic Computing,” *Journal of Materials Chemistry C* 13 (2025): 12046–12065, https://doi.org/10.1039/D5TC01467K.

7. Y. Gao, Z. Zhang, X. Ma, et al., “Fully Solution-Processed Flexible and Self-Rectifying Memristor for Synapse Emulation,” *ACS Applied Electronic Materials* 7, no. 5 (2025): 2075–2083, https://doi.org/10.1021/acsaelm.4c02323.

8. J. Feng, Y. Fan, Y. Wang, et al., “Stable Halide Perovskite Memristor Utilizing Innovative Silver/Bismuth Electrode as an Alternative to Gold,” *Advanced Functional Materials* 35, no. 24 (2025): 2420547, https://doi.org/10.1002/adfm.202420547.

9. M. M. H. Tanim, Z. Templin, and F. Zhao, “Natural Organic Materials Based Memristors and Transistors for Artificial Synaptic Devices in Sustainable Neuromorphic Computing Systems,” *Micromachines* 14, no. 2 (2023): 1–26, https://doi.org/10.3390/mi14020235.

10. J. Choi, S. H. Lee, T. Kim, K. Min, and S. N. Lee, “Enhanced Resistive Switching and Conduction Mechanisms in Silk Fibroin-Based Memristors With Ag Nanoparticles for Bio-Neuromorphic Applications,” *Nanomaterials* 15, no. 7 (2025): 517, https://doi.org/10.3390/nano15070517.

11. D. Hachim, O. Hernandéz-Cruz, J. E. J. Foote, et al., “Self-Doped and Biodegradable Glycosaminoglycan-PEDOT Conductive Hydrogels Facilitate Electrical Pacing of iPSC-Derived Cardiomyocytes,” *Advanced Healthcare Materials* 14, no. 9 (2025): e2403995, https://doi.org/10.1002/adhm.202403995.

12. A. Dan, D. Sharma, H. Singh, et al., “A Dynamically Crosslinked, Self-Adapting, Injectable Gelatin–Chondroitin Sulfate Hydrogel With Antibacterial and Antioxidant Properties for Treatment of Deep and Irregular Wounds,” *Journal of Materials Chemistry B* 13 (2025): 7293–7310, https://doi.org/10.1039/D4TB02537G.

13. J. J. Young, K. M. Cheng, Y. A. Young, et al., “Chondroitin Sulfate-Stabilized Silver Nanoparticles: Improved Synthesis and Their Catalytic, Antimicrobial, and Biocompatible Activities,” *Carbohydrate Research* 457 (2018): 14–24, https://doi.org/10.1016/j.carres.2017.12.004.

14. S. O. Ogungbesan, E. Buxaderas, R. A. Adedokun, et al., “Synthesis and Characterization of Chitosan–Silver Nanocomposite Film: Antibacterial and Cytotoxicity Study,” *ChemistrySelect* 9 (2024): e202404909, https://doi.org/10.1002/slct.202404909.

15. H. H. Ibrahim, A. M. Abdelghany, M. H. Gaber, and S. A. Ali, “Optical and Physical Characteristics of Chitosan/Silver Vanadate Nanocomposites,” *Optical and Quantum Electronics* 56 (2024): 435, https://doi.org/10.1007/s11082-023-05979-z.

16. R. Borah, R. Ninakanti, S. Bals, and S. W. Verbruggen, “Plasmon Resonance of Gold and Silver Nanoparticle Arrays in the Kretschmann (Attenuated Total Reflectance) vs. Direct Incidence Configuration,” *Scientific Reports* 12 (2022): 15738, https://doi.org/10.1038/s41598-022-20117-7.

17. U. Holzwarth and N. Gibson, “The Scherrer Equation Versus the Debye-Scherrer Equation,” *Nature Nanotechnology* 6 (2011): 534, https://doi.org/10.1038/nnano.2011.145.

18. M. Zhao, R. Li, and J. Xue, “Atomic Bridge Memristor Based on Silver and Two-Dimensional GeSe,” *AIP Advances* 10, no. 4 (2020): 045003, https://doi.org/10.1063/5.0002082.

19. V. A. Hernández, “An Overview of Surface Forces and the DLVO Theory,” *ChemTexts* 9 (2023): 10, https://doi.org/10.1007/s40828-023-00182-9.

20. D. J. Pochapski, C. Dos Santos Carvalho, G. W. Leite, S. H. Pulcinelli, and C. V. Santilli, “Zeta Potential and Colloidal Stability Predictions for Inorganic Nanoparticle Dispersions: Effects of Experimental Conditions and Electrokinetic Models on the Interpretation of Results,” *Langmuir* 37, no. 45 (2021): 13379–13389, https://doi.org/10.1021/acs.langmuir.1c02056.

21. B. Sun, Y. Chen, M. Xiao, et al., “A Unified Capacitive-Coupled Memristive Model for the Nonpinched Current–Voltage Hysteresis Loop,” *Nano Letters* 19, no. 9 (2019): 6461–6465, https://pubs.acs.org/doi/10.1021/acs.nanolett.9b02683.

22. S. Kim, C. Du, P. Sheridan, W. Ma, S. Choi, and W. D. Lu, “Experimental Demonstration of a Second-Order Memristor and Its Ability to Biorealistically Implement Synaptic Plasticity,” *Nano Letters* 15, no. 3 (2015): 2203–2211, https://doi.org/10.1021/acs.nanolett.5b00697.

23. A. Khanas, C. Hebert, D. Hrabovsky, L. Becerra, and N. Jedreci, “Universal Synaptic Plasticity of Interface-Based Second-Order Memristors,” *Advanced Electronic Materials* 10, no. 6 (2024): 2300803, https://doi.org/10.1002/aelm.202300803.

24. L. Zhang, N. Ge, J. J. Yang, R. S. Williams, and Y. Chen, “Low Voltage Two-State-Variable Memristor Model of Vacancy-Drift Resistive Switches,” *Applied Physics A* 119 (2015): 1–9, https://doi.org/10.1007/s00339-015-9033-3.

25. S. Kim, H. D. Kim, and S. J. Choi, “Compact Two-State-Variable Second-Order Memristor Model,” *Small* 12, no. 24 (2016): 3320–3326, https://doi.org/10.1002/smll.201600088.

26. A. Gabbitas, D. P. Pattnaik, Z. Zhou, and P. Borisov, “Resistive Switching Study on Diffusive Memristors Using Electrochemical Impedance Spectroscopy,” *Journal of Physics D: Applied Physics* 56, no. 30 (2023): 305102, https://doi.org/10.1088/1361-6463/acd06c.

27. K. Krishnan, M. Aono, and T. Tsuruoka, “Kinetic Factors Determining Conducting Filament Formation in Solid Polymer Electrolyte Based Planar Devices,” *Nanoscale* 8, no. 29 (2016): 13976–13984, https://doi.org/10.1039/C6NR00569A.

28. D. Lelmini and V. Milo, “Physics-Based Modeling Approaches of Resistive Switching Devices for Memory and In-Memory Computing Applications,” *Journal of Computational Electronics* 16, no. 4 (2017): 1121–1143, https://doi.org/10.1007/s10825-017-1101-9.

29. A. V. Toropin, L. Huang, V. R. Nikitenko, and O. V. Prezhdo, “Extremely Non-Equilibrium Hopping Transport and Photogeneration Efficiency in Organic Semiconductors: An Analytic Approach,” *Journal of Physical Chemistry Letters* 15, no. 14 (2024): 3884–3892, https://doi.org/10.1021/acs.jpclett.4c00662.

30. Z. Wang, S. Joshi, S. Savel'ev, et al., "Memristors With Diffusive Dynamics as Synaptic Emulators for Neuromorphic Computing," *Nature Materials* 16 (2017): 101–108, https://doi.org/10.1038/nmat4756.

31. J. B. Roldán, E. Miranda, D. Maldonado, et al., "Variability in Resistive Memories," *Advanced Intelligent Systems* 5, no. 6 (2023): 2200338, https://doi.org/10.1002/aisy.202200338.

32. S. Aldana and H. Zhang, "Unravelling the Data Retention Mechanisms Under Thermal Stress on 2D Memristors," *ACS Omega* 8, no. 30 (2023): 27543–27552, https://doi.org/10.1021/acsomega.3c03200.

33. S. Subramanian, N. Tiwale, K. Kisslinger, and C. Y. Nam, "Reduced Stochastic Resistive Switching in Organic–Inorganic Hybrid Memristors by Vapor-Phase Infiltration," *Advanced Electronic Materials* 8, no. 9 (2022): 2200172, https://doi.org/10.1002/aelm.202200172.

34. A. Marunchenko, J. Kumar, A. Kiligaridis, et al., "Charge Trapping and Defect Dynamics as Origin of Memory Effects in Metal Halide Perovskite Memlumors," *Journal of Physical Chemistry Letters* 15, no. 24 (2024): 6256–6265, https://doi.org/10.1021/acs.jpclett.4c00985.

35. A. Gubicza, M. Csontos, A. Halbritter, and G. Mihály, "Resistive Switching in Metallic Ag$_2$S Memristors due to a Local Overheating Induced Phase Transition," *Nanoscale* 7 (2015): 11248–11254, https://doi.org/10.1039/C5NR02536B.

36. T. Liu and D. E. Jiang, "Understanding the Interaction Between Carboxylates and Coinage Metals From First Principles," *Journal of Chemical Physics* 155, no. 3 (2021): 034301, https://doi.org/10.1063/5.0053045.

37. P. Colomban and G. Lucazeau, "Vibrational Study of and Conduction Mechanism in β Alumina. I. Stoichiometric β Alumina," *Journal of Chemical Physics* 72, no. 2 (1980): 1213–1224, https://doi.org/10.1063/1.439264.

38. Q. Huang, D. Qin, and Y. Xia, "Seeing Is Believing: What Is on the Surface of Silver Nanocrystals Suspended in Their Original Reaction Solution," *Chemical Science* 15 (2024): 6321–6330, https://doi.org/10.1039/D4SC00730A.

39. S. V. Adichtchev, M. V. Das'ko, L. L. Sveshnikova, et al., "Low-Frequency Raman Scattering of Light by Silver Nanoparticles," *Optoelectronics, Instrumentation and Data Processing* 49, no. 3 (2013): 287–292, https://doi.org/10.3103/S8756699013030102.

40. V. Mankad, K. K. Mishra, S. K. Gupta, T. R. Ravindran, and P. K. Jha, "Low Frequency Raman Scattering From Confined Acoustic Phonons in Freestanding Silver Nanoparticles," *Vibrational Spectroscopy* 61 (2012): 183–187, https://doi.org/10.1016/j.vibspec.2012.02.004.

41. S. Dirkmann, M. Ziegler, M. Hansen, H. Kohlstedt, J. Trieschmann, and T. Mussenbrock, "Kinetic Simulation of Filament Growth Dynamics in Memristive Electrochemical Metallization Devices," *Journal of Applied Physics* 118, no. 21 (2015): 214501, https://doi.org/10.1063/1.4936107.

42. X. Zhao, J. Xu, D. Xie, et al., "Natural Acidic Polysaccharide-Based Memristors for Transient Electronics: Highly Controllable Quantized Conductance for Integrated Memory and Nonvolatile Logic Applications," *Advanced Materials* 33, no. 52 (2021): 2104023, https://doi.org/10.1002/adma.202104023.

43. V. Profant, C. Johannessen, E. W. Blanch, P. Bouř, and V. Baumruk, "Effects of Sulfation and the Environment on the Structure of Chondroitin Sulfate Studied via Raman Optical Activity," *Physical Chemistry Chemical Physics* 21, no. 14 (2019): 7367–7377, https://doi.org/10.1039/C9CP00472F.

44. S. G. Elci, S. Rana, R. L. Phillips, et al., "Recognition of Glycosaminoglycan Chemical Patterns Using an Unbiased Sensor Array," *Chemical Science* 4, no. 5 (2013): 2047–2051, https://doi.org/10.1039/C3SC22187F.

45. Y. Ma, M. Wei, X. Zhang, T. Zhao, X. Liu, and G. Zhou, "Spectral Study of Interaction Between Chondroitin Sulfate and Nanoparticles and Its Application in Quantitative Analysis," *Spectrochimica Acta, Part A: Molecular and Biomolecular Spectroscopy* 153 (2016): 445–450, https://doi.org/10.1016/j.saa.2015.08.045.

46. K. Yan, Z. Zhang, M. Zhang, et al., "Resonance-Induced Anomalies in Temperature-Dependent Raman Scattering of PdSe$_2$," *Journal of Materials Chemistry C* 12, no. 30 (2024): 11402–11411, https://doi.org/10.1039/d4tc02012j.

47. A. Philip and A. R. Kumar, "The Performance Enhancement of Surface Plasmon Resonance Optical Sensors Using Nanomaterials: A Review," *Coordination Chemistry Reviews* 458 (2022): 214424, https://doi.org/10.1016/j.ccr.2022.214424.

48. D. Gokhfeld, M. R. Koblischka, and A. Koblischka-Veneva, "New Model to Predict Thermomagnetic Properties of Nanostructured Magnetic Compounds," *Applied Physics A* 131, no. 1 (2025): 21, https://doi.org/10.1007/s00339-024-08131-0.

Supporting Information

Additional supporting information can be found online in the Supporting Information section. **Figure S1:** UV–Vis absorption spectrum of Ag@ChS recorded in the 300–600 nm range at 25 °C, showing a distinct surface plasmon resonance (SPR) band centered at 418 nm. The relatively narrow full width at half maximum (FWHM) of ~80 nm indicates high monodispersity and size uniformity of Ag (●) nanoparticles, reflecting effective stabilization by the chondroitin sulfate matrix. **Figure S2:** XRD pattern of the Ag@ChS OMEMRs device recorded at room temperature (25 °C), confirming the crystalline phases in the nanocomposite structure. **Figure S3:** Zeta potential (ζ) of Ag nanoparticles measured at 25 °C, indicating the surface charge and colloidal stability of the dispersion. **Figure S4:** (a) I–V characteristic curve of the Ag@ChS OMEMRs recorded at 25 °C, showing non-pinched hysteresis indicative of second-order memristive dynamics. (b) Schematic diagram of the Ag@ChS OMEMRs device architecture. (c) Conceptual representation of the linear drift model, where device length is *D*. The Ag@ChS-doped region has instantaneous thickness *W(t)* and resistance $R_1 = R_{ON}$, while the undoped ChS region has thickness *(D—W(t))* and resistance $R_2 = R_{\text{OFF}}$. The total resistance is $R_{eq} = R_1 + R_2$. This model captures the dynamic modulation of conductive filament length under external bias, reflecting the coupled ionic/electronic processes governing second-order memristive behavior. **Figure S5:** jrs70039-sup-0005-Figure_S5.tif. *Temperature-dependent I–V characteristics of Ag@ChS OMEMRs*. The curves show how increasing temperature modulates charge transport and resistive switchin. Elevated temperatures enhance carrier mobility and reduce the high resistance state (HRS) by altering interfacial barriers and promoting Ag$^+$ and oxygen vacancy diffusion. A sharp drop in conductivity occurs above ~170 °C, indicating thermal degradation onset. **Figure S6:** Three-dimensional surface plot of the current response I(V, T) for the Ag@ChS memristor, as a function of voltage (V) and temperature (T). The color scale represents the output current intensity (A), highlighting conduction enhancement regions associated with thermal phase transition and field-driven effects. **Figure S7:** jrs70039-sup-0007-Figure_S7.tif. *Temperature-dependent evolution of the resistance ratio (R_{OFF}/R_{ON}) in Ag@ChS OMEMRs during forward and backward voltage sweeps.* **Figure S8:** jrs70039-sup-0008-Figure_S8.tif. *Retention performance of Ag@ChS OMEMRs over a 100-h period under forward and backward voltage sweeps at 25 °C*. Retention deviation index (RDI) and normalized noise (σ_{norm}) are used to quantify the stability of the low resistance state (R_{ON}) and high resistance state (R_{OFF}). **Figure S9:** Comparative radar chart of selected organic memristive devices, including the Ag@ChS-based OMEMRs (this work) and literature-reported devices [1, 2]. The performance metrics considered are the ON/OFF resistance ratio, data retention time, and operating voltage. All parameters were normalized to facilitate comparative visualization across heterogeneous device architectures. **Figure S10:** *Temperature-dependent attenuation of the Amide I (1600 cm^{-1}) Raman band in Ag@ChS OMEMRs.* The integrated band area was fitted using a Boltzmann-type sigmoidal function with ±1σ uncertainty envelope obtained via bootstrap resampling. The model captures the cooperative nature of thermally activated bond cleavage, molecular rearrangements, and vibrational decoherence in the hybrid matrix. **Figure S11:** Temperature-dependent attenuation of the sulfate (1150 cm^{-1}) Raman band in Ag@ChS OMEMRs. The integrated band area was modeled using a Boltzmann-type sigmoidal fit, with ±1σ confidence bounds derived from bootstrap resampling. The nonlinear decay reflects progressive desulfation and structural disintegration of the chondroitin sulfate framework under thermal stress.